

# Analysis of Unsteady Aerodynamics of a Car Model in Dynamic Pitching Motion Using LS-DYNA<sup>®</sup> R7

Yusuke Nakae, Tsuyoshi Yasuki, Hiroshi Tanaka, Jiro Takamitsu  
*Toyota Motor Corporation*

## Abstract

*This paper describes the numerical analysis of unsteady aerodynamics of a car model in dynamic pitching motion using LS-DYNA R7. Large-Eddy simulations with ALE method were performed to clarify the effects of unsteady aerodynamic forces on aerodynamic characteristics of cars in dynamic motion. The forced sinusoidal pitching oscillation was imposed on the 1/4 scaled car model and the flow velocity was set to 27.78 m/s. The model was based on a real production car and it was simplified by removing its engine compartment cavity and smoothing its surface. Tires were fixed on the ground and separated from the car body. Unsteady aerodynamic forces acting on the model were investigated. And the mechanism of the differences between the aerodynamic forces acting on the car model in the dynamic motion and those in stationary states occur was mainly discussed.*

*The computational results showed good agreement with the results of the high accuracy LES code computations. Also, results showed the differences between the aerodynamic forces in the dynamic pitching motion and those in the stationary states. Especially, the lift force showed remarkable differences. Even in the same posture of the pitch angle 0 degree (i.e. the posture in which the under floor of the car body is parallel to the ground), the lifts showed different values at stationary state and during nose-up or nose-down respectively.*

*As a result of this analysis, it was revealed that these differences in the aerodynamic forces were mostly due to the changes of the surface pressure distributions around rear end of the front wheelhouse. The flow structures behind the front tires changed with volume shrinking or expanding of front wheel house owing to the car motion. These changes affected the surface pressure distributions.*

## 1. Introduction

Flow fields around vehicles are known to affect various performance attributes such as fuel efficiency or dynamic performance. This has led to various studies being conducted on flow fields and various vehicle performance attributes. Those attributes have primarily been evaluated based on steady aerodynamic characteristics measured in wind tunnel tests while the vehicle was either stationary or subjected to a uniform flow. Recently, however it is becoming clear that the unsteady aerodynamic forces produced when a vehicle is in motion affect vehicle dynamic performance. In fact, by imposing pitching and heaving on a scale model in wind tunnel tests, Ascbwanden et al. [1] have shown that the unsteady aerodynamic forces acting on the model differed greatly from the steady ones. They then suggested that analyses taking unsteady aerodynamic forces into account would be required to improve vehicle stability and handling characteristics. Okada et al. [2] investigated two sedan type passenger vehicles in which steady aerodynamic characteristics were equivalent, but straight-line stability differed. They clarified that this difference was affected by the difference in the unsteady flow field structure above the trunk deck. Although various experimental researches are being conducted, discerning the details of flow field structures in experiments is difficult. Consequently, the particulars of unsteady flow fields and of their impact on vehicle dynamic performance have yet to be clarified.

Numerical simulation is expected to prove effective in shedding light on the detailed mechanism of unsteady flow fields around vehicles in dynamic motion. Cheng et al. [3] have applied the Arbitrary Lagrangian-Eulerian (ALE) method to a Large-Eddy Simulation (LES) and

conducted a numerical analysis of unsteady flow fields in the pitching motion of a simplified model simulating a vehicle. Tsubokura et al. [4] introduced yawing motion and lateral translation to the method presented by Cheng et al. [3] and performed an analysis which yielded a shape closer to that of an actual vehicle. Through an analysis of unsteady flow fields in the pitching and lane change motions of a simplified car model simulating the relative tire-body motions of a car in motion, Nakae et al. [5] clarified the mechanism by which aerodynamic parts mounted on the body side sill affect unsteady flow fields around the car model. As shown by these examples, the basic mechanism underlying unsteady flow fields around a vehicle in dynamic motion are gradually coming to light. However, such numerical research primarily relies on academic CFD codes, which often involves an enormous cost due to factors such as the large scale of the computations and the time they require. Moreover, in terms of robustness, there are still unresolved issues in terms of applying these academic CFD codes to product development.

In light of these factors, the LS-DYNA Incompressible CFD solver (ICFD), which includes Fluid-Structure Interaction (FSI) functionality, is expected to prove useful. Sawamoto et al. [6] applied the LS-DYNA ICFD solver to the analysis of unsteady flow fields around an Ahmed body model in pitching motion, and demonstrated that computational results showed good agreement with the experimental values.

This study adapts the method proposed by Sawamoto et al. [6] to the analysis of unsteady flow fields in the pitching motion of a 1/4 scale car model. It then validates the results through comparisons with those obtained by Nakae et al. [5]. In addition, it compares computational results in dynamic and stationary cases and discusses the mechanisms that generate unsteady aerodynamic forces.

## 2. Object of this study

The 1/4 scale car model used in this study is shown in Fig. 1. The model was obtained by smoothing the body surface relative to that of the actual vehicle, and by removing elements such as the engine compartment, underside components, and the suspension. The model has a total length ( $L$ ) of 1057 mm, a width ( $W$ ) of 441 mm and a height ( $H$ ) of 373 mm. The tires and body are independent, and the variations in the gap between the wheel houses and the tires when the vehicle is in dynamic motion were simulated (see Fig. 2).

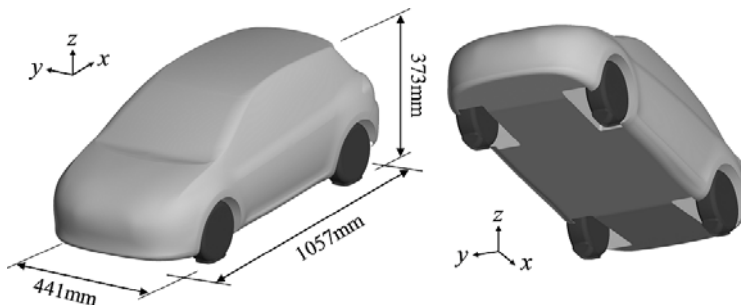


Fig. 1 1/4 scale car model

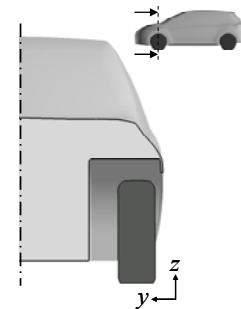
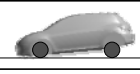
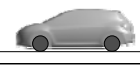
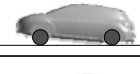


Fig. 2 Section view of wheel house

Table 1 shows the simulation cases. The simulation cases were made for three cases of stationary state and a pitching motion case. In all cases, mainstream velocity was 27.78 m/s, and the Reynolds number, which is based on the total length of the model, was  $Re = 1.91 \times 10^6$ . To represent the pitching motion, forced sinusoidal pitching oscillation was imposed on the body

using the center of the wheel base as the center of rotation (see Fig. 3). The mechanism producing unsteady aerodynamic forces was discussed by comparing the results of the above simulations for the dynamic and stationary states of the model.

Table 1 List of simulation case

	Motion	Pitch angle $\theta$	Velocity	$Re^*$	Schematic view
Case 1	<b>Stationary state</b>	$-1.32^\circ$	27.78 m/s	1.91 $\times 10^6$	
Case 2		$0^\circ$			
Case 3		$+1.32^\circ$			
Case 4	<b>Pitching oscillation</b> Frequency 5.5Hz	$\pm 1.32^\circ$			

\* Reynolds number based on the model length  $L$

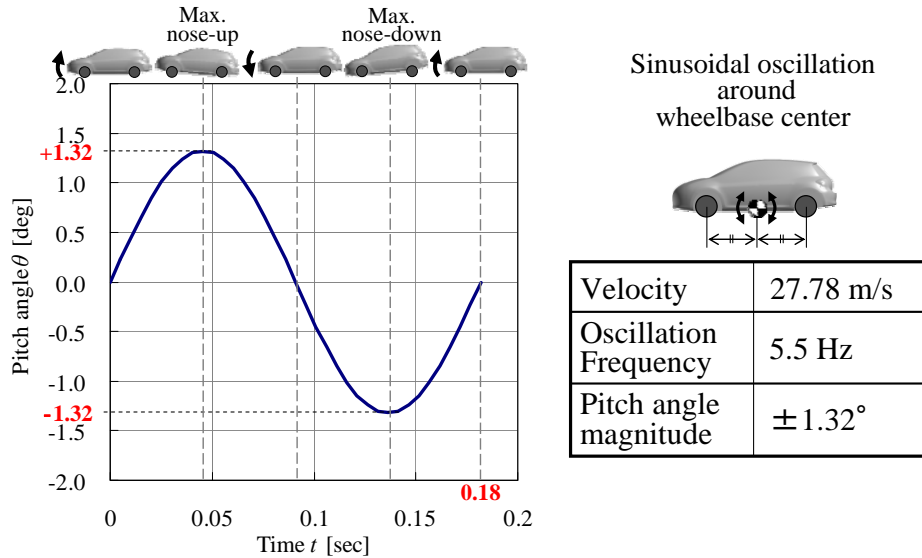


Fig. 3 Behavior of model in pitching oscillation (Case 4)

### 3. Numerical methods

This study used the ICFD solver in LS-DYNA R7. A Large-Eddy Simulation (LES) was used to model turbulent components. And the Arbitrary Lagrangian-Eulerian (ALE) method was used to represent the model motion. A spatially filtered Navier-Stokes equation (1) and a mass continuity equation (2) were used as the governing equations,

$$\rho \left( \frac{\partial \tilde{U}_i}{\partial t} + (\tilde{U}_j - v_j) \frac{\partial \tilde{U}_i}{\partial x_j} \right) = - \frac{\partial \tilde{P}}{\partial x_i} + \frac{\partial}{\partial x_j} \left[ \mu \frac{\partial \tilde{U}_i}{\partial x_j} + \mu_{sgs} \frac{\partial \tilde{U}_i}{\partial x_j} \right] \quad (1)$$

$$\frac{\partial \tilde{U}_i}{\partial x_i} = 0 \quad (2)$$

where  $t$ ,  $x_i$ ,  $U_i$ ,  $v_i$ ,  $P$ ,  $\rho$ , and  $\mu$  respectively represent, time, coordinate components, velocity components, grid movement velocity components, pressure, air density, and the viscosity

coefficient. Variables marked with a  $\sim$  symbol are spatially filtered, which means that they are grid scale component variables. Further,  $\mu_{sgs}$  is the sub grid scale turbulent eddy viscosity coefficient and modeled by the Smagorinsky model shown in equation (3). The Smagorinsky constant  $C_S$  used in this study is 0.18.

$$\mu_{sgs} = \rho(C_S f_v \Delta)^2 \sqrt{2\tilde{S}_{ij}\tilde{S}_{ij}} \tag{3}$$

$$C_S = 0.18 \tag{4}$$

In the above equations, the rate of strain tensor  $S_{ij}$  and the Van Driest wall damping function  $f_v$ ,  $\Delta$  are defined as below.

$$\tilde{S}_{ij} = \frac{1}{2} \left( \frac{\partial \tilde{U}_j}{\partial x_i} + \frac{\partial \tilde{U}_i}{\partial x_j} \right) \tag{5}$$

$$f_v = 1 - \exp\left(\frac{-y^+}{25}\right) \tag{6}$$

$$\Delta = (\textit{element volume})^{\frac{1}{3}} \tag{7}$$

The  $y^+$  is the non-dimensional wall distance.

The fractional step method was used to solve the equations.

### 4. Numerical conditions

Fig. 4 shows the computational domain. Dimensions are indicated in reference to  $L$ , the total length of the model. Flow direction is  $10L$ , width direction is  $2L$  and height direction is  $1.5L$ . Fig. 5 shows the model surface and the computational grid in its vicinity. The computational grid for the model surface has a resolution of approximately 4 mm, and a 5-layer boundary layer mesh was inserted in the model surface as well as in the floor of the computational domain. The first layer has an approximate height of  $y^+ = 3.5$ . The entire computational domain consists of unstructured tetrahedral grids using a total of 11.5 million elements and 1.9 million nodes.

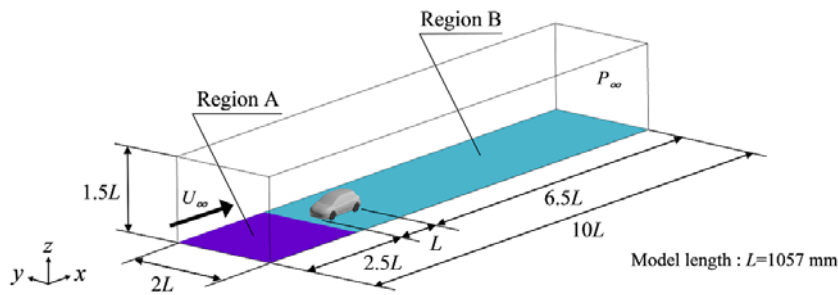


Fig. 4 Computational domain

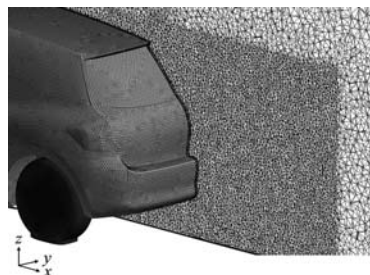


Fig. 5 Close-up view of computational grid

Boundary conditions are presented in Table 2. They are the same across all simulation cases.

Table 2 List of boundary condition

Boundary	Condition
Inlet	Uniform velocity $U_{\infty}= 27.78$ [m/s]
Outlet	Constant pressure $P_{\infty}= 0$ [Pa]
Floor	Region A : Free-slip, Region B : Non-slip
Side walls, Ceiling	Free-slip
Model surface	Non-slip, 5 layers of boundary layer meshes

## 5. Results

In this section, the computational results for aerodynamic forces in Case 1 through 4 are shown. And the validity of the present computational methods is shown through comparisons with the results found in the literature [5].

### 5.1 Stationary cases (case 1 through 3)

Fig. 6 shows the computational results for steady aerodynamic forces in a stationary state. They indicate the time averaged values for 0.7 second after sufficient convergence was applied to the calculations. They showed good agreement with the results of the high accuracy LES code computations found in the literature [5], which were themselves obtained from academic CFD codes and using a computational grid with 48 million elements and 11 million nodes. Divergences of the magnitude from the results in the literature [5] were observed in the lift coefficient  $C_L$  and drag coefficient  $C_D$ , but both showed a consistent close correspondence in the change of value due to the different pitch angle. The lift coefficient  $C_L$  rose as the pitch angle increased. By contrast, the drag coefficient  $C_D$  did not exhibit changes comparable to those of the  $C_L$  relative to pitch angle changes.

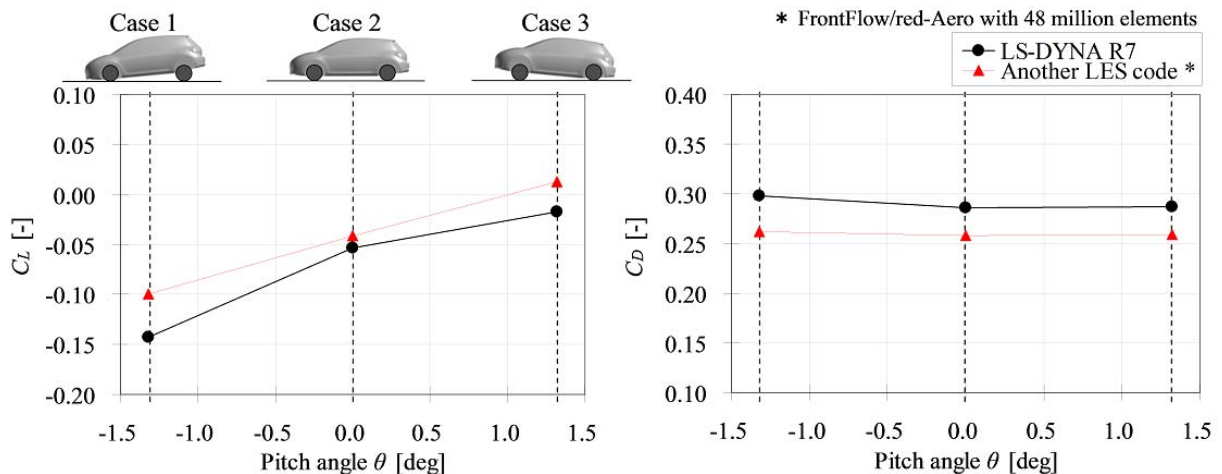


Fig. 6 Steady aerodynamic characteristics at stationary states : Case 1, 2, 3  
(left : lift coefficient  $C_L$ , right : drag coefficient  $C_D$ )

### 5.2 Dynamic case (case 4)

Fig. 7 shows the computational results for unsteady aerodynamic force during pitching motion. The result indicates the phase averaged value for five cycles after sufficient convergence was applied to the calculation, and also the result of the computation found in the literature [5] is presented. This report focuses on the lift coefficient  $C_L$ , in which pronounced unsteadiness in aerodynamic forces relative to vehicle dynamic motion was observed. The  $C_L$  during pitching motion showed good agreement with the results from the literature [5], the magnitude, and the trends extremely closely, all of which suggests that the results obtained through the present computational method largely reproduce flow field phenomena and are valid. One notable point is that even for the same  $0^\circ$  pitch angle, aerodynamic forces exhibit significant differences during nose-up and nose-down, and also show considerable differences in the stationary state (i.e., unsteady aerodynamic force). At the same pitch angle of  $0^\circ$ , the  $C_L$  was higher during nose-up (Fig. 7 (1)) than in the stationary state (Fig. 7 (2)). By contrast, the  $C_L$  was lower during nose-down at a pitch angle of  $0^\circ$  (Fig. 7 (3)) than in the stationary state at a pitch angle of  $0^\circ$  (Fig. 7 (2)). This indicates that even if the vehicle is in the same posture in both the stationary and dynamic states, the aerodynamic forces acting on the vehicle differ and, additionally, that even during dynamic motion, aerodynamic forces vary if the direction of motion differs.

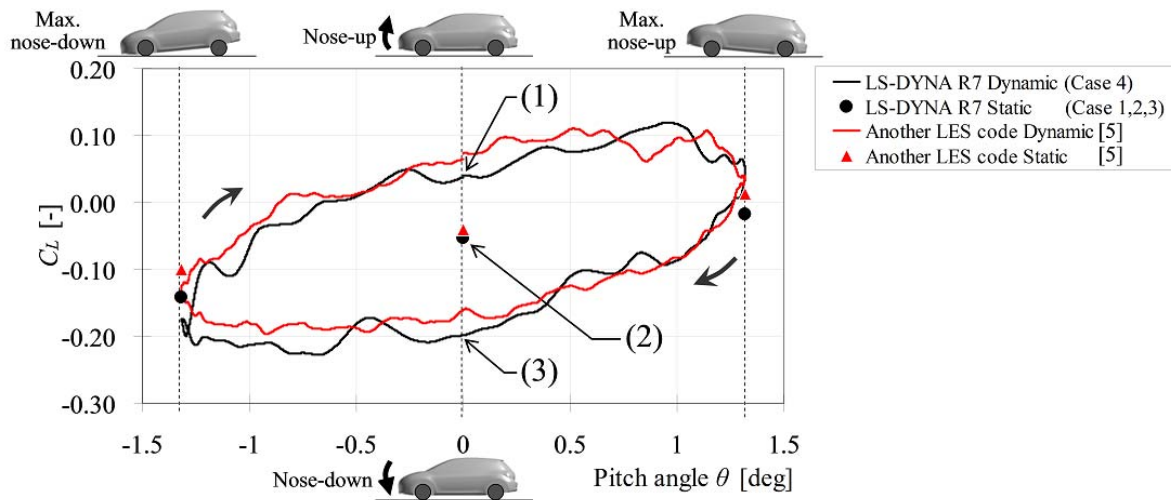


Fig. 7 Unsteady aerodynamic force during pitching motion and steady aerodynamic force

To pinpoint the cause of the above-mentioned differences in aerodynamic force, the  $C_L$  acting on each part of the model body for nose-up at pitch angle  $0^\circ$  ((1) in Fig. 7), stationary state at pitch angle  $0^\circ$  ((2) in Fig. 7), and nose-down at pitch angle  $0^\circ$  ((3) in Fig. 7) are presented in Fig.8. These results revealed that the differences in aerodynamic force  $C_L$  is generated most remarkably behind the rear end of the Fr wheel house on the lower surface of the model body (FLR-2,3,4).

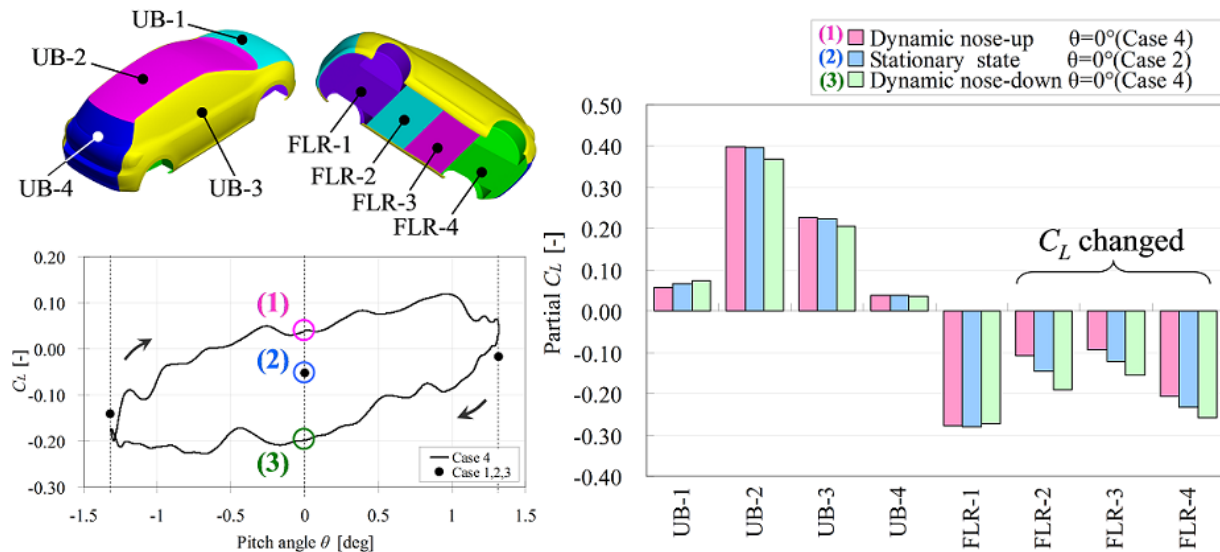


Fig. 8 Aerodynamic force  $C_L$  acting on each part of model body

## 6. Discussion

In this section, it examines the cause of the changes in the lift coefficient  $C_L$  obtained in the previous section 5 through comparisons of the surface pressure distributions and the flow fields around the model, the flow rate under the model.

### 6.1 Stationary cases (case 1 through 3)

This section examines the cause of the lift coefficient  $C_L$  increase that accompanies the rise in the pitch angle presented in Fig. 6. Fig. 9 shows the time averaged values of the distribution of the pressure coefficient  $C_P$  on the model surface for each pitch angle. For all pitch angles, almost no difference was observed on the upper surface of the model body. On the other hand, differences were observed on the lower surface of the model body. At pitch angle of  $-1.32^\circ$  (Case 1), an area with lower pressure compared to the other cases was observed from the front of the lower surface to the vicinity of the rear end of the Fr wheel house. Compared to Case 1, the exact opposite trend was observed at a pitch angle of  $+1.32^\circ$  (Case 3), with the zone ranging up to the vicinity of the Fr wheel house exhibiting an area of higher pressure. At a pitch angle of  $0^\circ$  (Case 2), a distribution falling between that of Case 1 and Case 3 was observed. As a result, the lift coefficient  $C_L$  was lowest in Case 1, where vehicle body surface pressure drops. Conversely, it is highest in Case 3, where model body surface pressure rises. These results are probably due to the Venturi effect. In Case 1, where the pitch angle is  $-1.32^\circ$ , the front end of the lower surface of the model body comes closer to the ground, narrowing the path between the lower surface of the model body and the ground, which increases flow velocity and decreases pressure. In Case 3, where the pitch angle is  $+1.32^\circ$ , the effect is reversed: the lower surface of the model body moves further away from the ground, widening the path between the lower surface of the model body and the ground, which decreases flow velocity and increases pressure. These likely accounts for the increase in lift coefficient  $C_L$  that accompanies the rise in pitch angle.

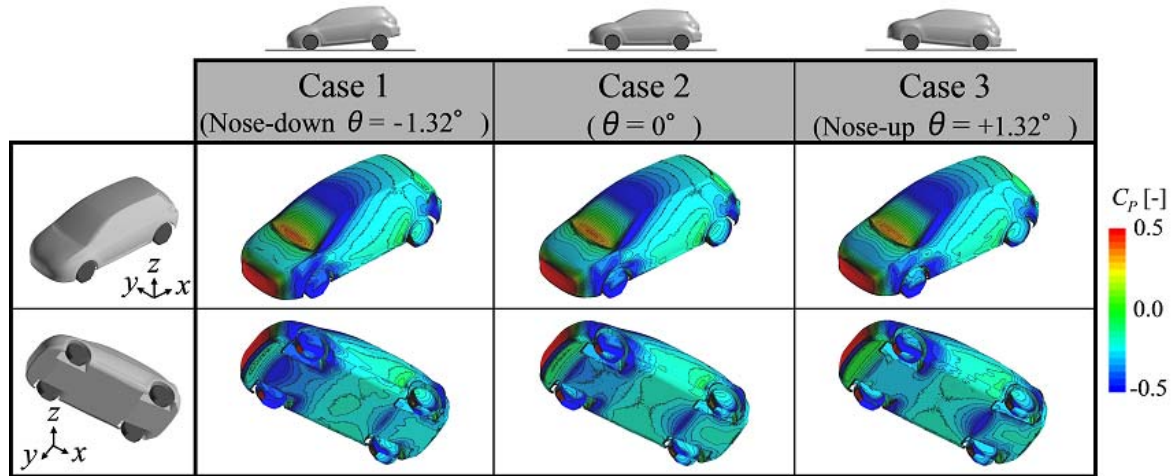


Fig. 9 Surface pressure distributions at each stationary case

### 6.2 Dynamic case (case 4) & Stationary case (case 2)

This section examines the causes underlying the differences in the  $C_L$  for different directions of motion despite identical vehicle postures, as well as the differences in the  $C_L$  between that in stationary state and that in pitching motion, presented in parts (1), (2) and (3) of Fig. 7. As shown in Fig. 8 these differences in aerodynamic force occur mainly on the lower surface of the model body. Consequently, the pressure coefficient  $C_p$  distributions for the lower surface of the model body for, respectively, (1) nose-up at pitch angle  $0^\circ$ , (2) stationary state at pitch angle  $0^\circ$ , and (3) nose down at pitch angle  $0^\circ$  are shown in Fig. 10. The values presented below are phased averaged values for (1) and (3), and time averaged values for (2). Remarkable differences in pressure distribution were observed behind the vicinity of the rear end of the Fr wheel house. A three-way comparison showed that pressure was highest during nose-up (1) and lowest during nose-down (3). The different results exhibited by the  $C_L$  despite identical vehicle postures are probably due to these variations in pressure.

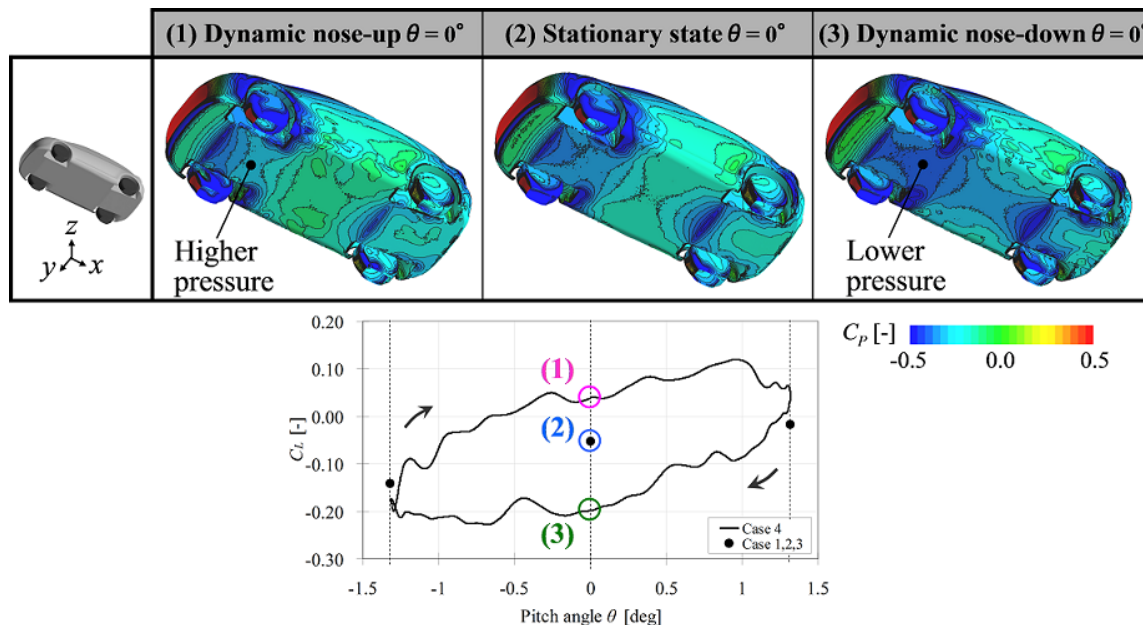


Fig. 10 Surface pressure distributions at pitch angle  $\theta = 0^\circ$  for different situations

Next comes an examination of the causes of the differences in the pressure distributions in the lower surface of the model body. Parts (1), (2) and (3) of Fig. 11 show the respective velocity magnitude distributions of the center cross-section in the direction of width ( $y = 0$ ). Remarkable differences in the flow velocity distributions were observed under the underside of the model body. A three-way comparison showed that flow velocity was slowest during nose-up (1) and fastest during nose-down (3). The higher pressure on the lower surface of the model body during nose-up (1) and a lower pressure during nose-down (3) are attributed to this effect.

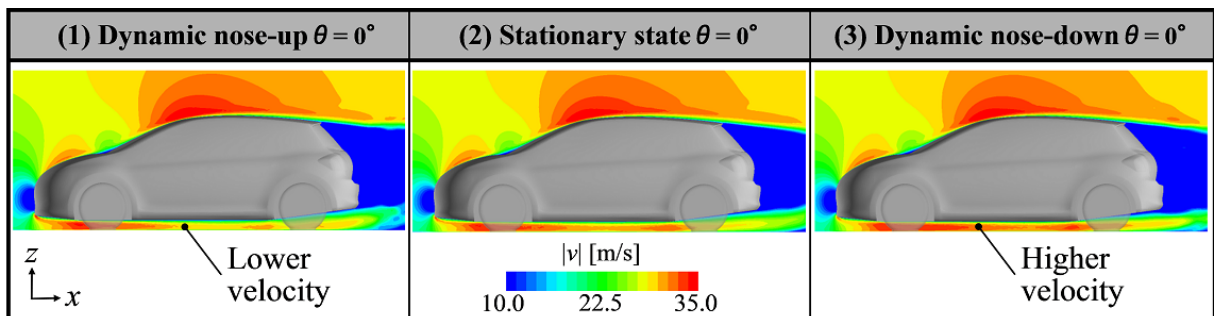


Fig. 11 Velocity magnitude distributions at  $y = 0$  at pitch angle  $\theta = 0^\circ$  for different situations

The causes of the differences in flow velocity on the underside of the vehicle body are examined next. Fig. 12 shows the volume flow rates under the model body underside for each parts (1), (2) and (3) respectively. Volume flow rate differences occurred behind the vicinity of the Fr wheel house. Comparing all three showed that the flow rate dropped most during nose-up (1) and, conversely, rose most during nose-down (3). The flow fields in the vicinity of the Fr wheel house at those points are shown in Fig. 13. During nose-up (1), when the flow rate in the vicinity of the Fr wheel house dropped, suction from the lower surface of the model body to the Fr wheel house was confirmed. In addition turbulence and decreased flow velocity was observed behind the Fr tire. By contrast, during nose-down (3), when the flow rate in the vicinity of the Fr wheel house rose, downward blowing from behind the Fr wheel house was confirmed, as was an increase in flow velocity behind the Fr wheel house. It is thought that these effects are caused by changes in the flow structures in the vicinity of Fr wheel house by changing the Fr wheel house volumes, which are due to the relative motions of the vehicle body and tires that accompany vehicle dynamic motion.

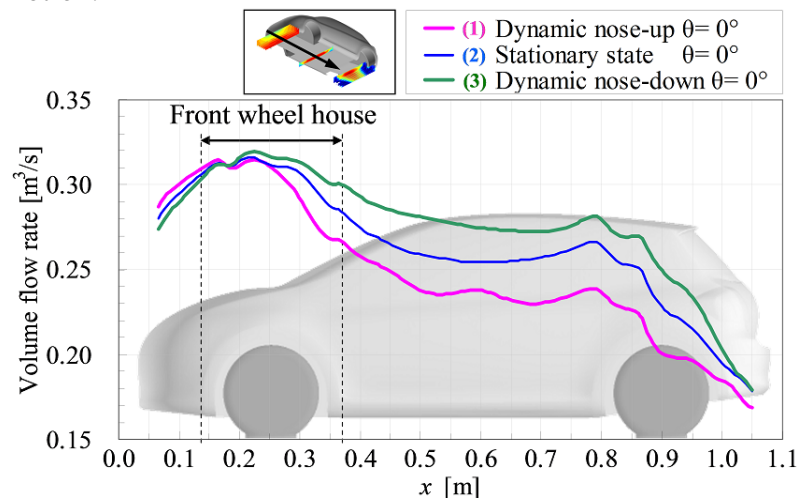


Fig. 12 Volume flow rate under model body at pitch angle  $\theta = 0^\circ$  for different situations

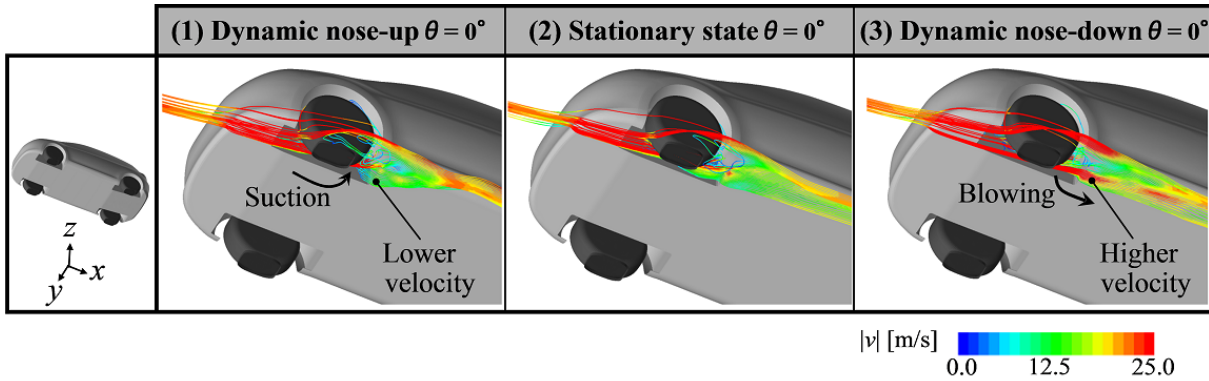


Fig. 13 Stream lines in vicinity of Fr wheel house at pitch angle  $\theta = 0^\circ$  for different situations

Parts (1), (2), and (3) of Fig. 14 show the respective vortical structures around the Fr wheel house. The vortex at the rear end of the Fr wheel house was observed to change with model dynamic motion. In particular, Vortex A exhibited strong evolution during nose-down (3). This corresponds to the downward blowing from the rear of the Fr wheel house observed in Fig. 13.

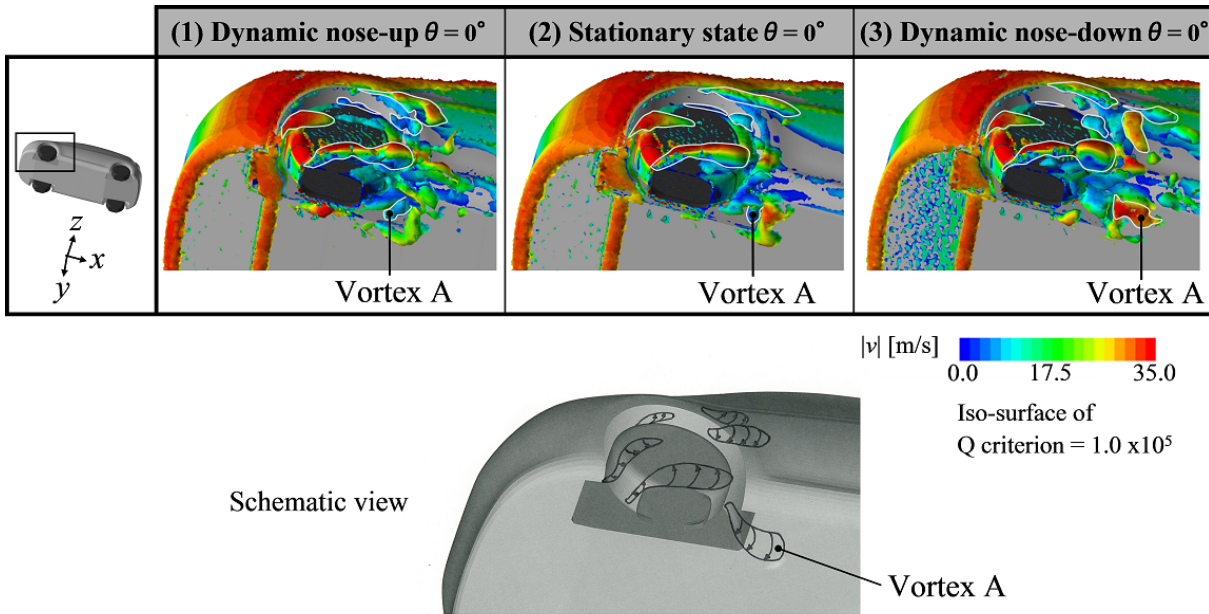


Fig. 14 Vortical structures in vicinity of Fr wheel house at pitch angle  $\theta = 0^\circ$  for different situations

Thus, the relative motion of the model body and tires causes the Fr wheel house volume to expand during nose-up, drawing the flow from the lower surface of the model body into the Fr wheel house. This makes flow velocity drop under the underside of the model body in the vicinity of the Fr wheel house, increasing the surface pressure on the body. Conversely, during nose-down, the Fr wheel house volume shrinks, blowing the flow from the Fr wheel house to the lower surface of the model body. This results in a higher flow velocity under the underside of the model body in the vicinity of the Fr wheel house, lowering surface pressure on the body. Therefore, even for the same model posture, the  $C_L$  differs depending on the direction of motion and, additionally, unsteady aerodynamic forces different from those in the stationary state are generated.

## 7. Conclusions

The numerical analysis of unsteady aerodynamics of a car model in dynamic pitching motion was conducted by using LS-DYNA R7. As a result of this analysis, the following were made clear.

- i. The computational results showed good agreement with the results by high accuracy LES code.
- ii. Differences in the aerodynamic forces between acting on car in dynamic motion and that in stationary state were confirmed.
- iii. The flow structures around the front wheel house that changed with car motion have affected the aerodynamic forces (i.e. unsteady aerodynamic forces).

## Acknowledgments

Thanks and appreciation are extended to extensive assistance and support with LS-DYNA provided by Mr. Amano, Mr. Mori and Mr. Hayashi of the JSOL Corporation over the course of this study.

## References

- [1] Aschwanden, P., et al., : The Influence of Motion Aerodynamics on the Simulation of Vehicle Dynamics, SAE Technical Paper, 2008-01-0657 (2008)
- [2] Okada, Y., et al., : Flow Structures above the Trunk Deck of Sedan-Type Vehicles and Their Influence on High-Speed Vehicle Stability 1st Report: On-Road and Wind-Tunnel Studies on Unsteady Flow Characteristics that Stabilize Vehicle Behavior, SAE Technical Paper, 2009-01-0004(2009)
- [3] Cheng, S.Y., et al., : A numerical analysis of transient flow past road vehicles subjected to pitching oscillation, Journal of Wind Engineering and Industrial Aerodynamics, Vol.99, p.511-522(2011)
- [4] Tsubokura, M., et al., : Unsteady Vehicle Aerodynamics during a Dynamic Steering Action: 2nd Report, Numerical Analysis, SAE Technical Paper, 2012-01-0448(2012)
- [5] Nakae, Y., et al., : A Study of Unsteady Aerodynamic Forces Acting on Car in Dynamic Motion, Transactions of Society of Automotive Engineers of Japan, Vol.44, No.6, 20134862(2013)
- [6] Sawamoto, H., : Unsteady Aerodynamic Analysis around Oscillating Ahmed body by LS-DYNA ver.980, 9th European LS-DYNA Conference(2013)